Supporting Information

Maximizing Piezoelectricity by Self-assembled Highly Porous Perovskite-Polymer Composite Films for Enabling the Internet of Things

Asif Abdullah Khan[a], Md Masud Rana[a], Guangguang Huang* [a], Nanqin Mei[b], Resul Saritas[c], Boyu Wen[a], Steven Zhang[a], Peter Voss[d], Eihab-Abdel Rahman[c], Zoya Leonenko[b], Sharif Islam[d], Dayan Ban*[a]

[a] Department of Electrical and Computer Engineering, University of Waterloo, 200 University Ave, Waterloo, ON, Canada

[b] Department of Physics & Astronomy, University of Waterloo, 200 University Ave, Waterloo, ON Canada

[c] Department of Systems Design Engineering, University of Waterloo, 200 University Ave, Waterloo, ON Canada

[d] Shimco North America Inc., 75 Heroux Devtek Dr, Cambridge, ON, Canada

Email: g43huang@uwaterloo.ca, dban@uwaterloo.ca

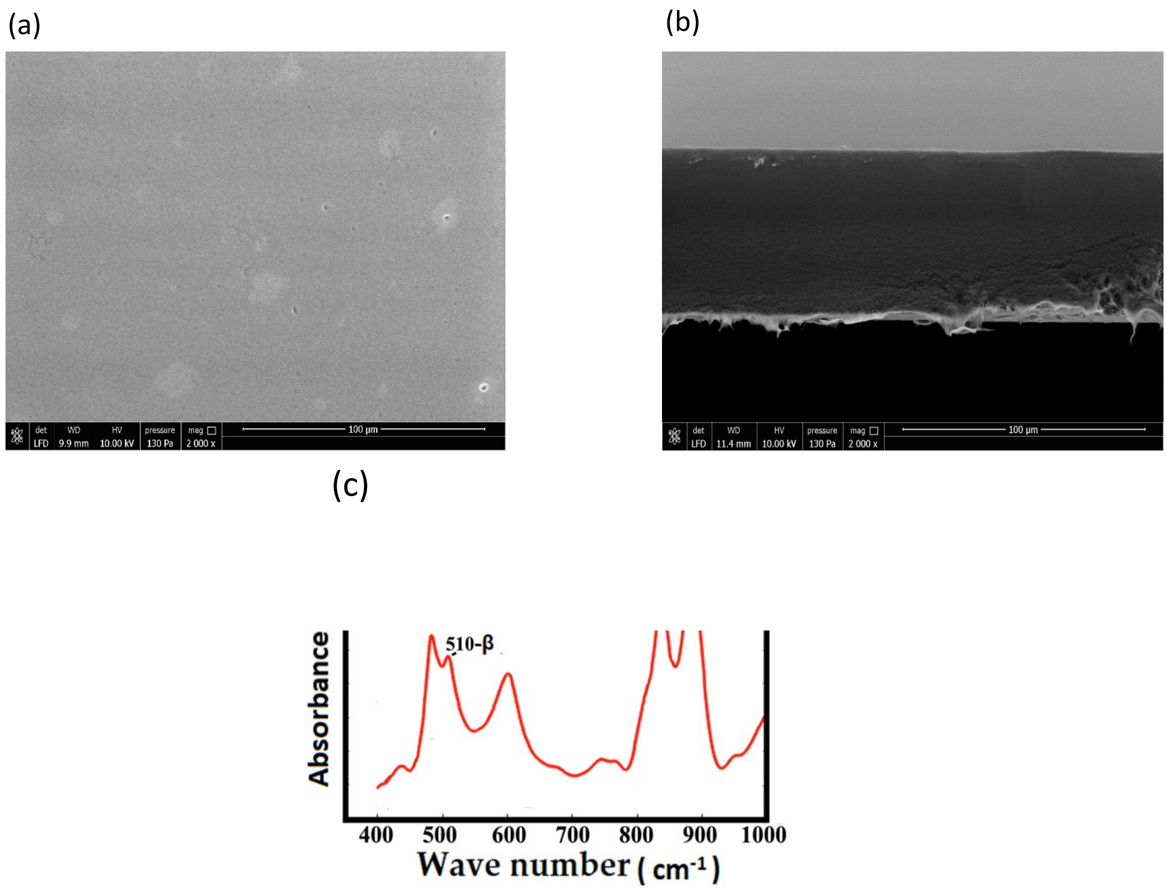

Fig. S1 The characterization of the pure PVDF film. Scanning electron microscopy (SEM) image of (a) top surface of the pure PVDF (annealed at 75 °C) (b) the cross section of the pure PVDF film. The SEM images indicate that the surface of the pure PVDF is uniform (c) FTIR spectrum of the PVDF film is indicating the β-phase formation (corresponding absorptions at the wavenumbers of 510 cm^{-1}, and 841 cm^{-1}).

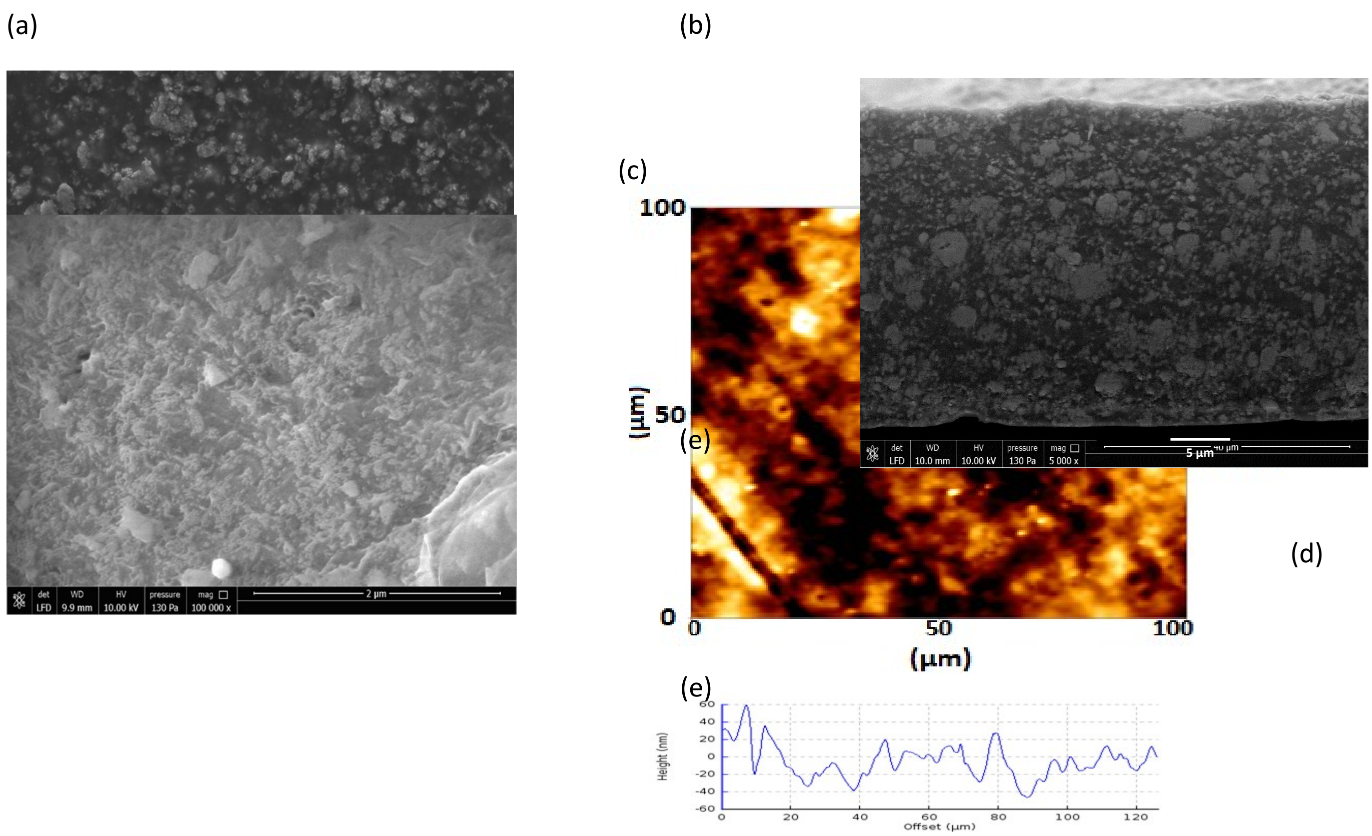

Fig. S2 The characterization of the porous PVDF film (a) top surface SEM image of the PVDF loaded with ZnO nanoparticles(NPs) with a diameter of 35-45 nm (b) cross sectional SEM image of the PVDF loaded with ZnO NPs. The SEM images are indicating that nanoparticles are not uniformly distributed rather accumulated in different positions of the PVDF film. This creates pores of different sizes after an etching process (c) top surface SEM image of the porous PVDF film obtained after the etching of ZnO NPs by 37 wt. % hydrochloric acid (HCl) (d) atomic force microscopy (AFM) image of the porous PVDF surface (e) measured surface roughness of the porous PVDF (≈ 100 nm)

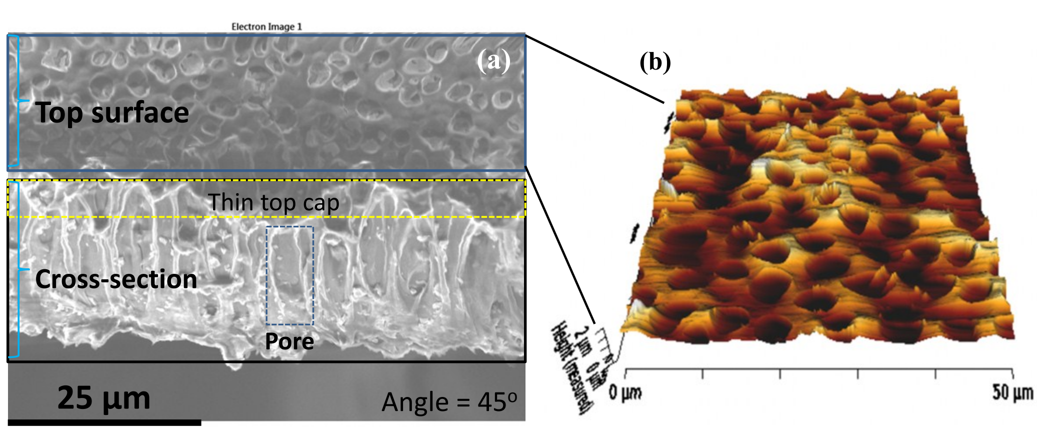

Fig. S3 The morphology of pore structures in the P-PNGs (a) cross-sectional SEM image of the $FAPbBr_2I$@PVDF film shows that the pores with a length of 20-25 μm are regularly distributed here (b) surface topography of the $FAPbBr_2I$@PVDF film from the AFM image illustrates that the diameter of the pores are approximately 3-5 μm.

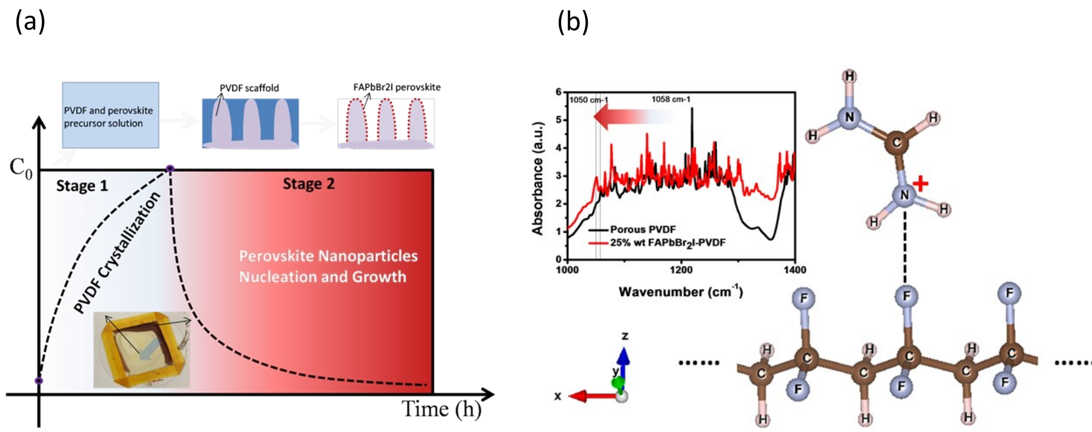

Fig. S4 (a) Schematic illustration of crystallization process of the PVDF and the $FAPbBr_2I$ nanoparticles. The y axis represents the total concentration of PVDF and $FAPbBr_2I$ in the solution (b) schematic demonstration shows the interactions between FA^+ cations and $-CF_2-$ groups. From the FTIR spectrum, this interaction is confirmed by the blue-shift of the infra-red absorption peaks of C-F bond in the wave number range of 1350-1100 cm^{-1}.

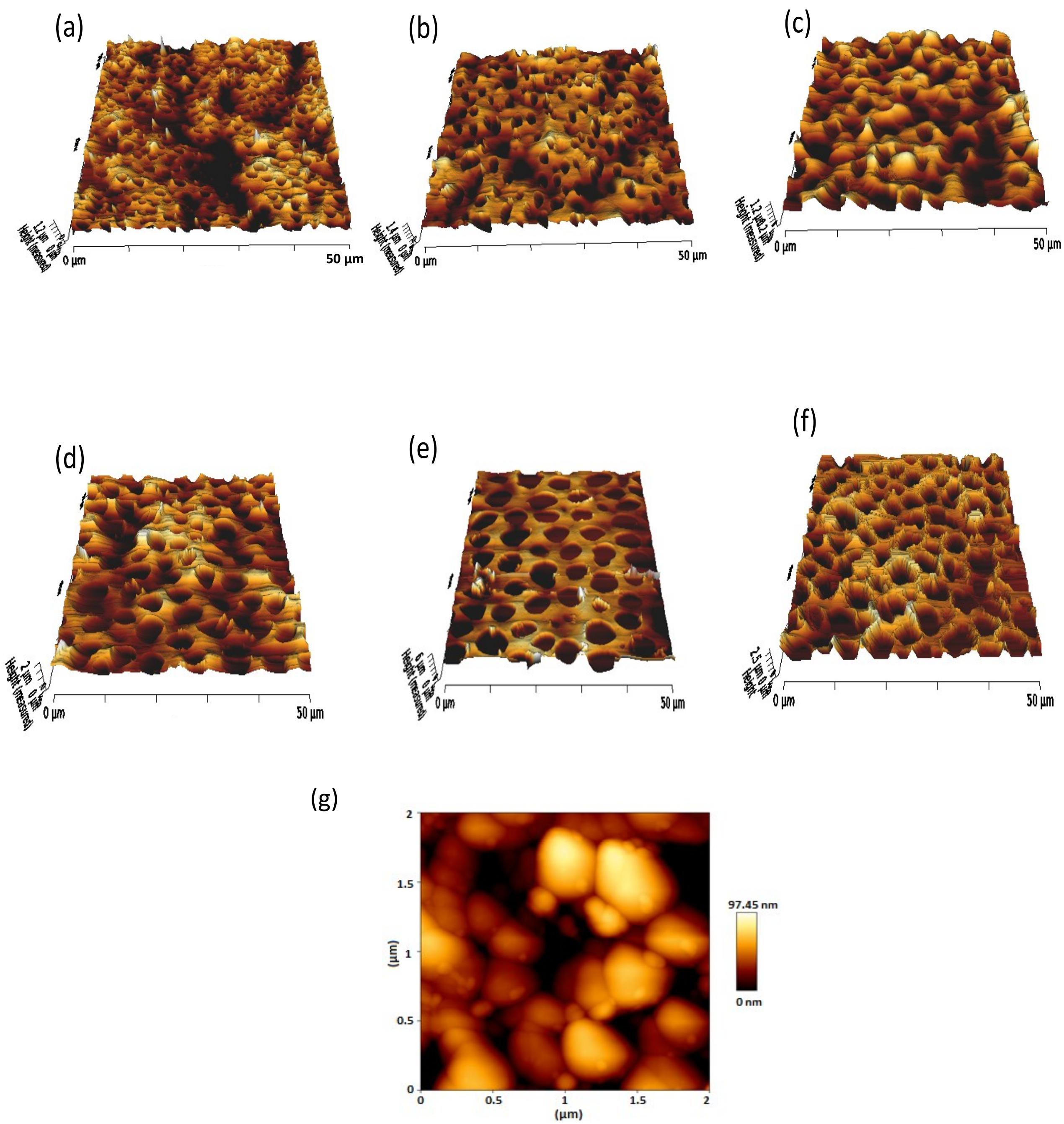

Fig. S5 The atomic force microscopy (AFM) images of PVDF-$FAPbBr_2I$ film with different mass ratios (wt. %) of $FAPbBr_2I$ precursor in 10 wt. % PVDF solution (a) 5 wt. % (b)10 wt. % (c) 15 wt. % (d) 20 wt. % (e) 25 wt. % (f) 30 wt. %. This AFM images clearly indicates the gradual increase in the pores size (diameter of up to 7 μm at 30 wt. % $FaPbBr_2I$) with the increase of $FAPbBr_2I$ concentration. Interestingly the pores are generated almost in the nature of a periodic array throughout the entire film (g) grain boundary topology of $FaPbBr_2I$ NPs ($\approx$ 100 nm).

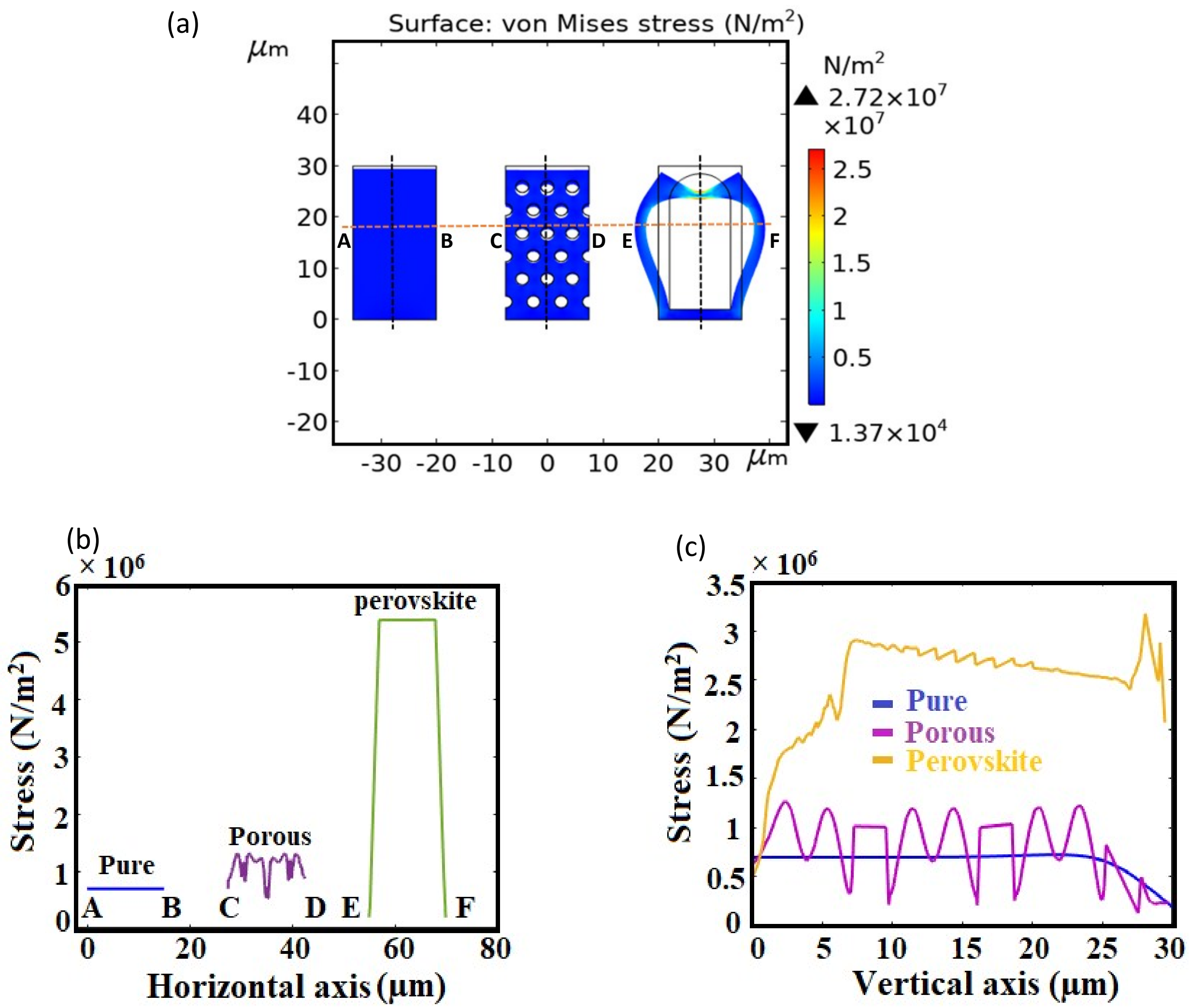

Fig. S6 (a) Finite element simulation of the pure, the circular porous and the highly porous perovskite-polymer films under a compressive pressure of 800 kpa. The mechanical stress is calculated (b) along the horizontal axis (A-F) (c) along the vertical axis, which clearly shows a higher stress in the film with a porous structure than the non-porous (pure) film. The stress distribution is disrupted by the presence of pores inside the film and further increases with the porosity.

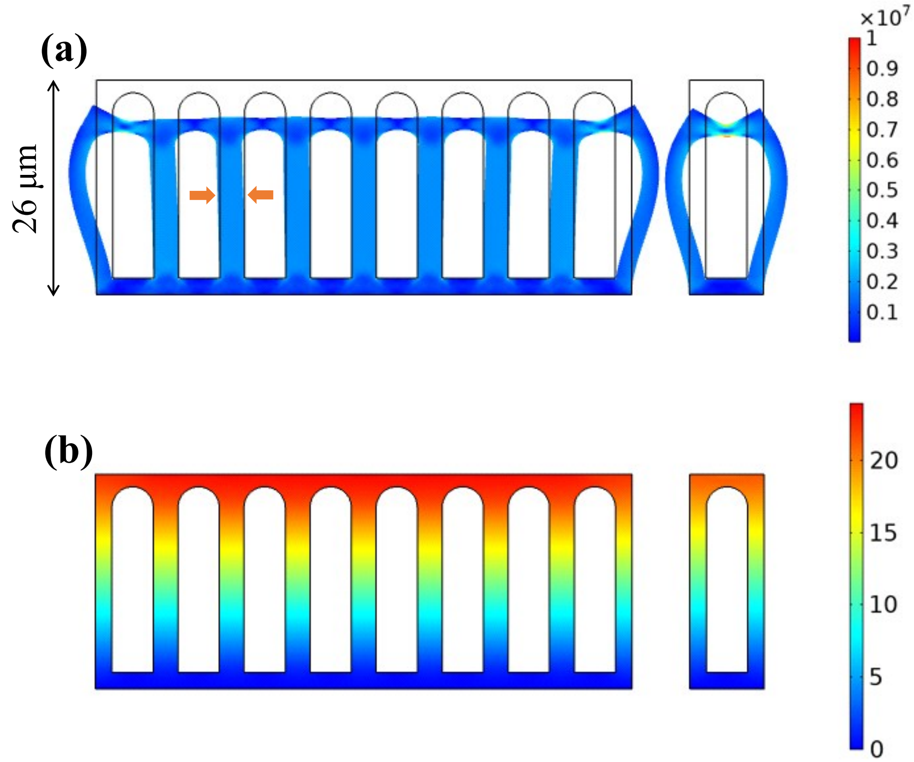

Fig. S7 A comparison of piezo-potential distribution for porous $FAPbBr_2I$@PVDF (20 wt. %) film with the presence of a single and an array of pore (8 pores) structures. The shape of the pores has been optimized from the observation of cross-section SEM image of the composite film. (a) Mechanical stress distribution of the film with the array of pores (left) and the film with a single pore (right) structure. The arrows are indicating the amplified stress on the sidewall of each pores. (b) The piezo-potential distribution is higher in the film with the presence of a large number of pore structures (left).

Note 1: Relationship between the piezoelectric charge coefficient and the strain

The behaviour of self-assembled porous perovskite-PVDF nanogenerator (NGs) can be analyzed by the fundamental piezoelectric equations. For the composite porous film in both mechanical and electrically equilibrium condition (no external force & no free charge density), the coupled constitutive law is,

$$\sigma_{ij} = C_{ijkl}^{E} S_{kl} - e_{nij} E_n \qquad (1)$$

$$D_m = e_{mkl} S_{kl} + k_{mn}^{\varepsilon} E_n \qquad (2)$$

Here, σ_{ij} and S_{kl} are the stress and strain, E_n and D_m are the electric field and electric displacement, respectively; and C_{ijkl}^{E}, e_{mkl}, $and\ k_{mn}^{\varepsilon}$ are the elastic (under a constant field), piezoelectric and dielectric tensor (under a constant stress).

For our P-PNG model, electric displacement (D_m) is strain (S_{kl}) dependent. As there is no applied electric field, equation (2) can be written as,

$$D_m = e_{mkl} S_{kl} \qquad (3)$$

Therefore, the electric displacement across the device thickness direction (along 3 –axis) is,

$$D_3 = e_{3kl}S_{kl} \qquad (4)$$

For the P-PNG model, according to the simulation, not only the strain S_{33} along the 3-axis is contributing to the electric-displacement, a significant amount of strain S_{31} along 1-axis is influencing the net electric displacement D_3. As a result, the equation (4) turns into,

$$D_3 = e_{333}S_{33} + |e_{331}|\, S_{31} \qquad (5)$$

Here, D_3= Q/A=CV/A (Q is charge, C is the device capacitance, V is the output voltage from device, A is the electrode area)

S_{33} can be written as, S_{33}= z/t (t is the device thickness, and z is the displacement along 3-axis);

And S_{31}= x/w (w is the device width, and x is the displacement along 1-axis).

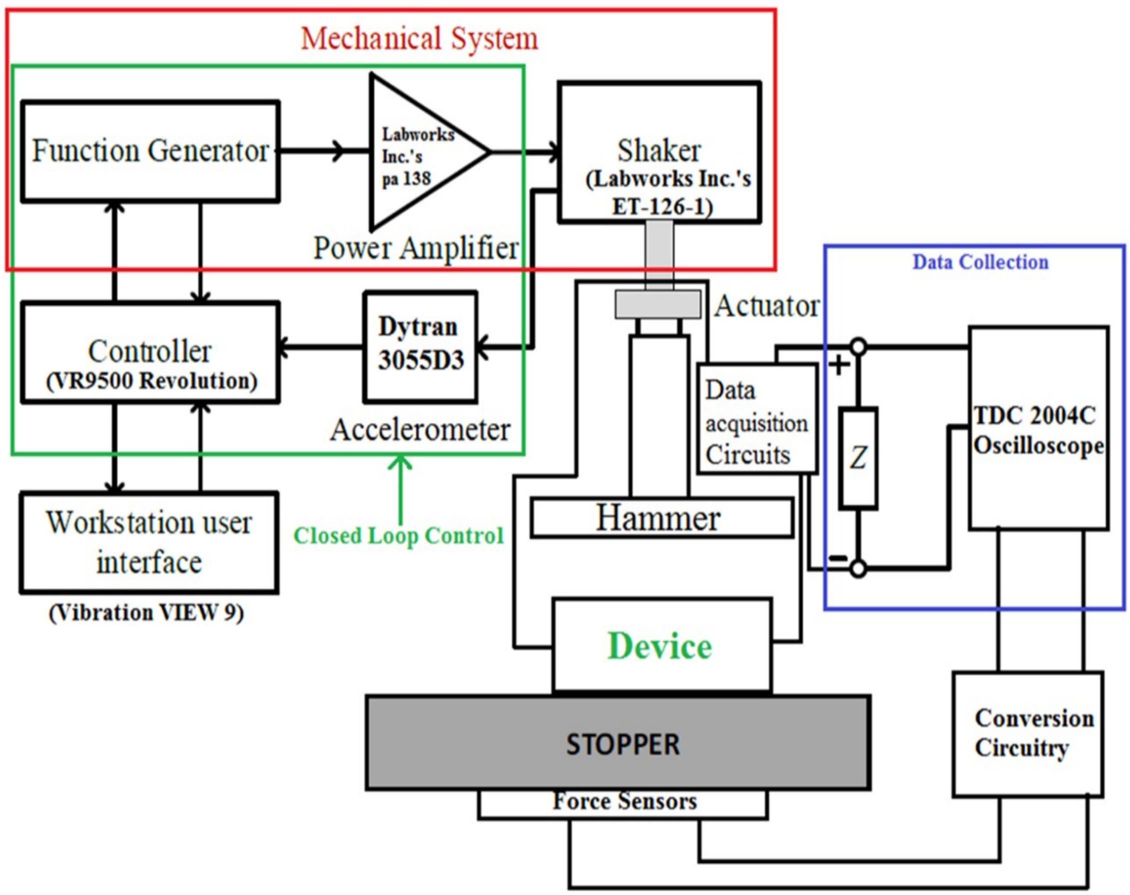

Fig. S8 A characterization system[64] of energy harvester. The controller unit is operated by a workstation interface (Vibration View 9). The controller unit (VR 9500) generates different control signals which are amplified by a power amplifier (Lab Works Inc.'s pa 138) to feed a electrodynamic shaker (ET-126-1) to control its motion. An accelerometer (3055D3) provides the feedback signal from the shaker to the controller unit which can take actions if there are any faults. The shaker is mechanically coupled with a metallic hammer to characterize the energy harvesting devices. The output from the devices are measured and viewed by an oscilloscope.

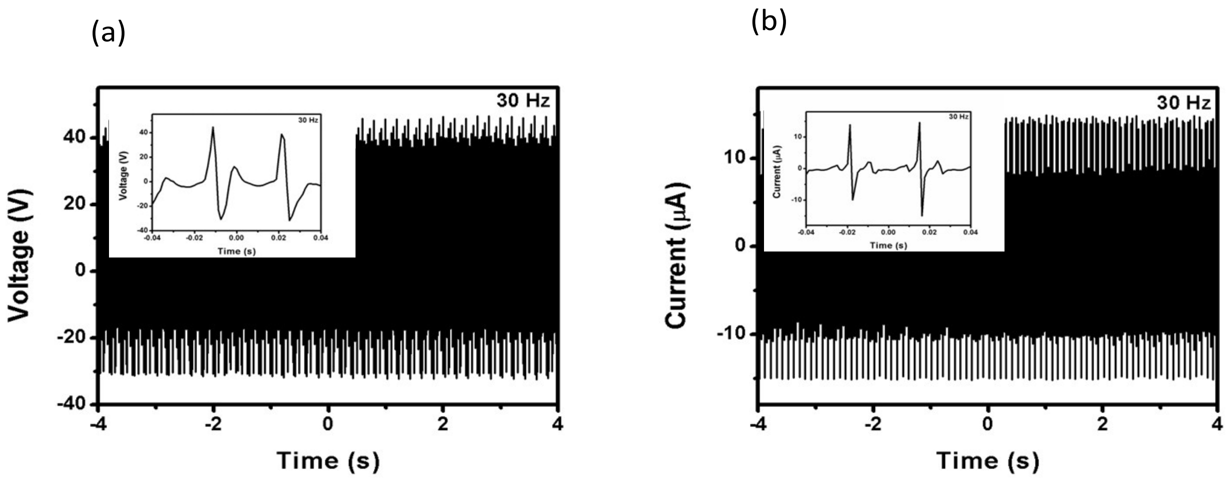

Fig. S9 Output performance of the P-PNGs. (a) output voltage and (b) current of the P-PNG at 30 Hz and 2G acceleration with an applied load of 138 gram (g).

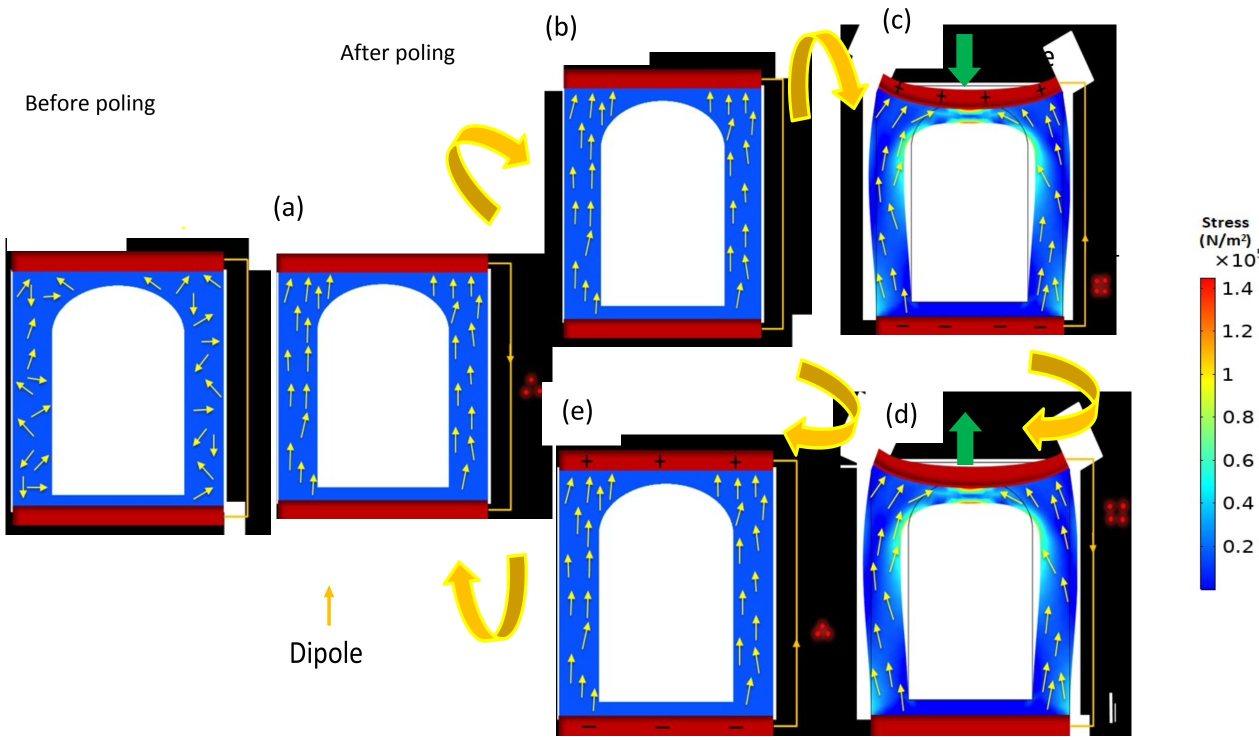

Fig. S10 Schematics of energy generation mechanisms of the P-PNGs based on distributed stress profile.

(a) (b)

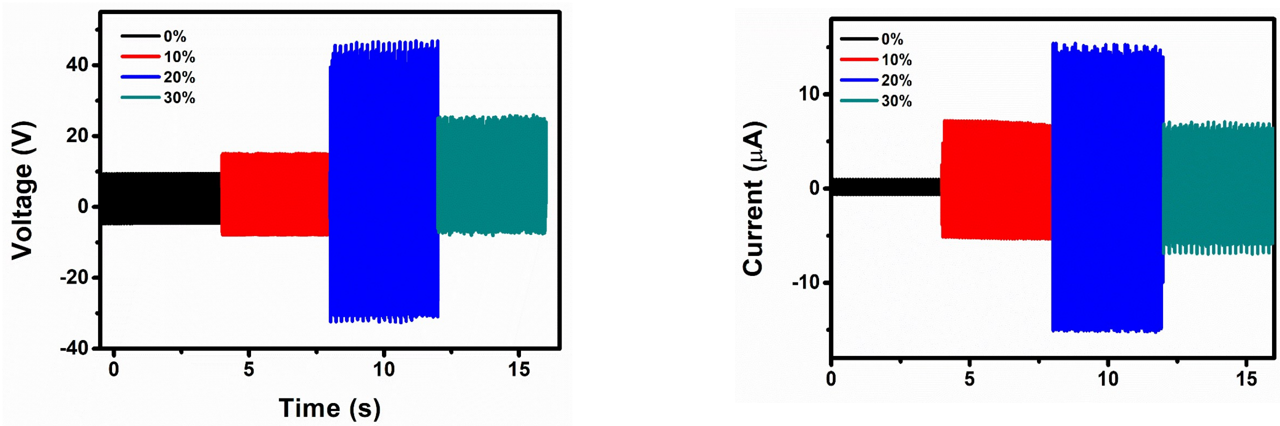

Fig. S11 Variation of output voltage (left) and output current (right) of the P-PNGs with different $FAPbBr_2I$ mass ratios (0 wt.%, 10 wt.%, 20 wt.%, 30 wt. %). The maximum output voltage (85 V) and current (30 μA) was obtained for 20 wt. % $FAPbBr_2I$@PVDF composite. The output voltage and current increases up to the mass ratio of 20 wt.%, and then decreases afterwards. The higher mass ratio of $FAPbBr_2I$ (> 20 wt. %) will generate very large pores to greatly reduce PVDF per unit volume and create more defects.

(a) (b)

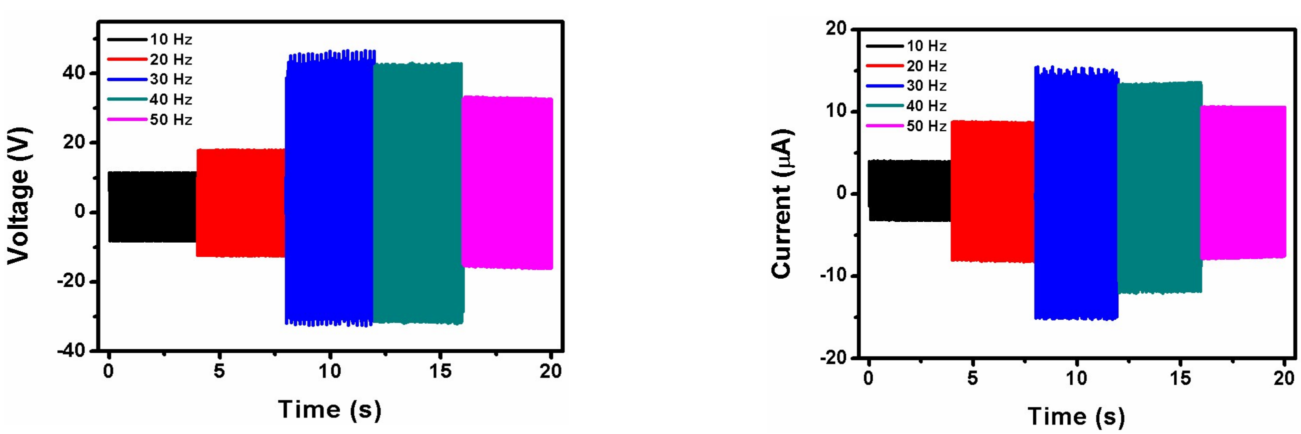

Fig. S12 Frequency dependent (10-50 Hz) output voltage (left) and output current (right) of the 20 wt. % $FAPbBr_2I$@PVDF based P-PNGs, when the acceleration is fixed at 2G. The maximum output voltage and output current at 30 Hz frequency was 85 V and 30 μA, respectively. As the frequency increases the strain rate rises and causing the increase in the output voltage and current. The gradual decrease in the output at higher frequencies (> 30 Hz) corresponds to the reduction of impact on the device by the 138 gram (g) proof mass.

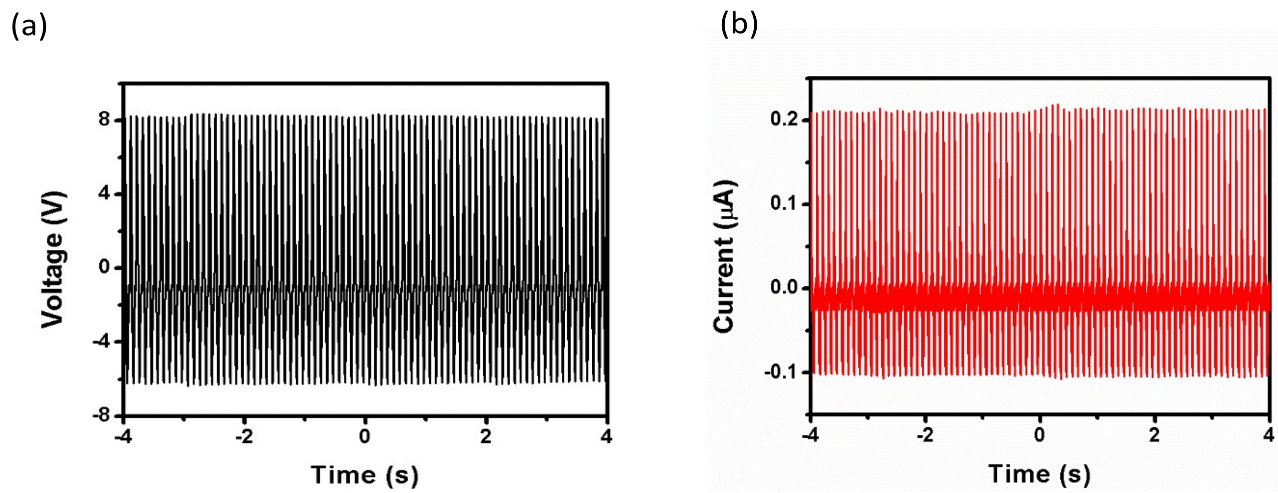

Fig. S13 Flexibility test of the P-PNGs at 10 Hz and 2G acceleration when a periodic bending force was applied from an electrodynamic shaker. The generated (a) output voltage (b) output current of 14 V and 0.3 μA, respectively, depicts the performance of the P-PNG during the bending condition.

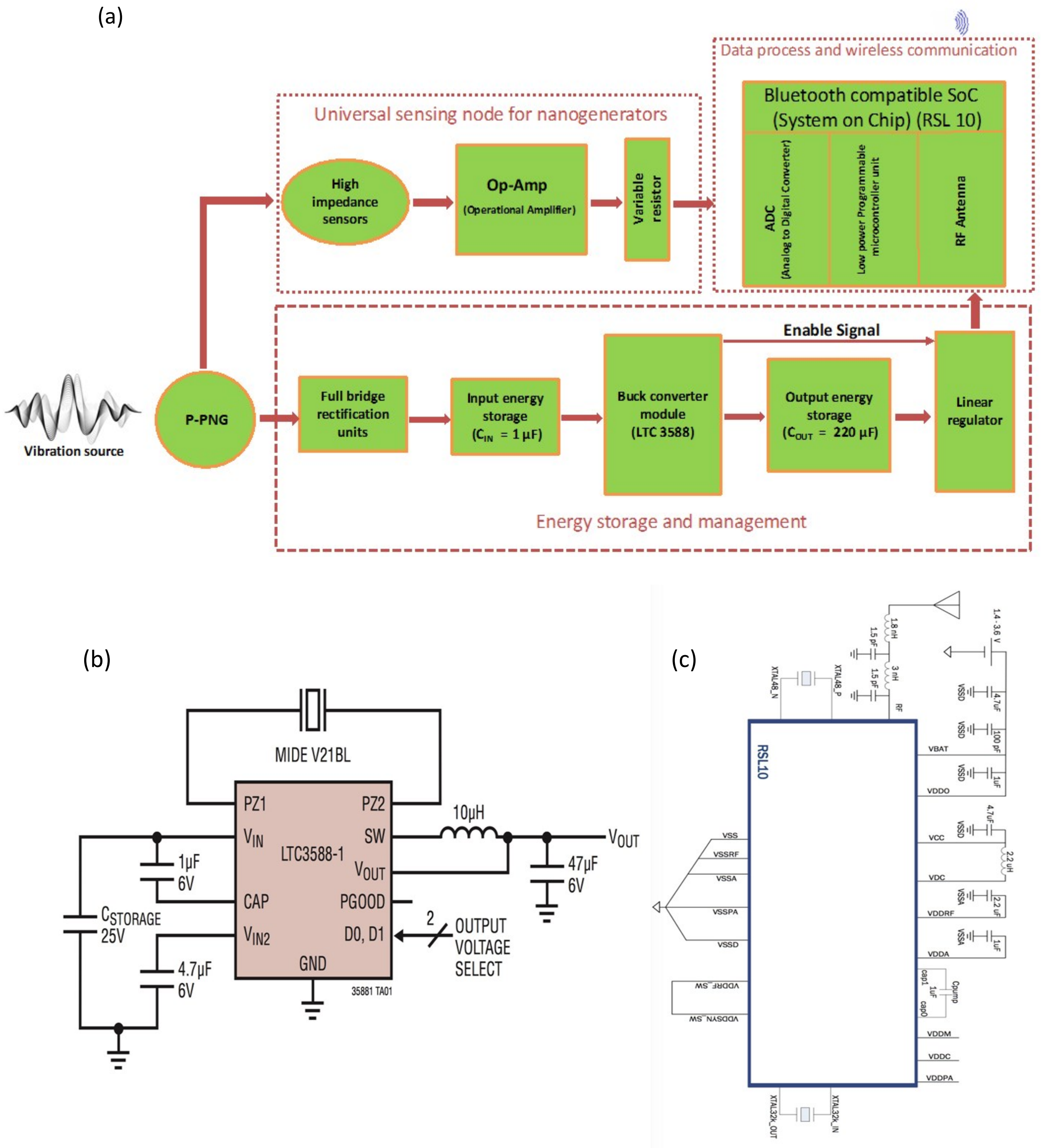

Fig. S14 Self Powered integrated wireless electronics node (SIWEN) (a) functional block diagram of the SIWEN (b) internal circuit diagram of a LTC 3588-1 module (c) architecture of a RSL-10 system on chip (SoC).

Note 2 : Descriptions of the self-powered integrated wireless electronics node (SIWEN)

To store and manage the energy harnessed by the P-PNGs, two-stage energy transfer mechanism was adopted. Following the rectification of the P-PNG output by using a schottky diode based full-bridge rectifier unit (**Fig. S14a**), rectified output was stored in an input capacitor of 1 µF. The output level of the input capacitor was regulated to $\approx$ 5 V. After the voltage level of the input capacitor reaches to 5 V, the stored electrical energy was transferred to the output capacitor of 220 µF (permanent storage) through a buck converter module (LTC 3588-1). The buck converter module operates at undervoltage-lockout mode (UVLO), which allows a certain portion of energy from the input storage to be transferred to the permanent storage. While transferring the energy through an inductor (10 µH) **(Fig. S14b)** to the output capacitor**,** a PMOS switch (p-type metal-oxide-semiconductor) inside the LTC-3588-1 module is used to ramping up the output current and a NMOS switch (n-type metal-oxide-semiconductor) is used to bring it down. This switching strategy provides a high output current to store electrical charges to the output capacitor. When the input capacitor's voltage falls below the UVLO threshold, the buck converter is turned off and input capacitor starts to store the charges again. The output voltage of the permanent storage capacitor is monitored by a V_{OUT} pin **(**circuit diagram in **Fig. S14b)** and compared with a pre-set regulation point (≈ 3 V) of a comparator (PGOOD). After reaching the output voltage level of the permanent storage to the set point, the buck converter generates a control signal (enable) through the PGOOD pin in **Fig. S14b** while entering into a sleep mode (≈ 100 nA of load current).

The enable signal in **Fig. S14a** switches a linear regulator (a digital switch), and energy from the output capacitor is transferred to a RSL-10 **(**architecture in **Fig. S14c)** system on chip (SoC). In the RSL-10, sensor's output signal is continuously sampled by an ADC (analog to digital converter), and the signal is processed to capture the peak value of the output and to transmit it to the remote receiver through a radio frequency link. As the nanogenerator based sensors (e.g. the P-PNG) possesses a high internal impedance (of megaohm range), it is challenging to integrate them with an existing commercial electronics node (e.g. RSL-10). Nevertheless, an Op-Amp (operational-amplifier) which operates at unity gain was designed as a interfacing unit between the sensor and RSL-10. When the magnitude of the enable signal reaches ≈ 92% of its peak value, linear regulator turns off, and buck- converter is disconnected from the output energy storage and input energy storage unit start to charge again by the P-PNG.

Table 1 A Comparison of output performance of the state-of-the-art PNG devices

Active material of PNGs	Film thickness (µm)	Applied force (N)/pressure (Mpa)	Frequency (Hz)	Output voltage (V)	Output current (µA)/current density (µA/cm²)	References
$FaPbBr_3$-PDMS	150	0.5 Mpa	7	8.5	3.8 µA/cm²	45
$NaNbO_3$-PDMS	100	[-]	<1	3.2	0.072 µA	28
PMN-PT-PDMS	150	Hand-tapping	5	7.8	2.29 µA	29
$FAPbBr_3$-PVDF	120	0.5 Mpa	5	30	6.2 µA/cm²	43
$MAPbBr_3$-PVDF	[-]	Finger tapping	2	5	0.06 µA	42
$MAPbI_3$-PVDF	6	0.5 Mpa	5	17.8	2.1 µA/cm²	44
PZT-NH_2/SM	200	[-]	<1	65	1.6 µA	41
$FAPbBr_2I$-PVDF	**30**	**1.35 N**	**30**	**85**	**30 µA**	**This work**